Cylindrical implosion platform for the study of highly magnetized plasmas at Laser MegaJoule

G. Pérez-Callejo,[1,2,*] C. Vlachos,[1,3] C. A. Walsh,[4] R. Florido,[5] M. Bailly-Grandvaux,[6] X. Vaisseau,[7] F. Suzuki-Vidal,[8] C. McGuffey,[9] F. N. Beg,[6] P. Bradford,[1] V. Ospina-Bohórquez,[1,7,10,11] D. Batani,[1] D. Raffestin,[1] A. Colaïtis,[1] V. Tikhonchuk,[1,12] A. Casner,[1,13] M. Koenig,[14] B. Albertazzi,[14] R. Fedosejevs,[15] N. Woolsey,[16] M. Ehret,[17] A. Debayle,[7,11] P. Loiseau,[7,11] A. Calisti,[18] S. Ferri,[18] J. Honrubia,[19] R. Kingham,[8] R. C. Mancini,[20] M. A. Gigosos,[2] and J. J. Santos[1,†]

[1]*Université de Bordeaux-CNRS-CEA, Centre Lasers Intenses et Applications (CELIA), UMR 5107, F-33405 Talence, France*
[2]*Departamento de Física Teórica, Atómica y Óptica, Universidad de Valladolid, 47011 Valladolid, Spain*
[3]*Institute of Plasma Physics & Lasers, Hellenic Mediterranean University Research Centre, 74100 Rethymno, Greece*
[4]*Lawrence Livermore National Laboratory, Livermore, California 94550, USA*
[5]*iUNAT–Departamento de Física, Universidad de Las Palmas de Gran Canaria, 35017 Las Palmas de Gran Canaria, Spain*
[6]*Center for Energy Research, University of California-San Diego, La Jolla, California 92093, USA*
[7]*CEA, DAM, DIF, F-91297 Arpajon, France*
[8]*Plasma Physics Group, The Blackett Laboratory, Imperial College London, London SW7 2AZ, United Kingdom*
[9]*General Atomics, San Diego, California 92121, USA*
[10]*University of Salamanca, 37008 Salamanca, Spain*
[11]*Université Paris-Saclay, CEA, Laboratoire Matière en Conditions Extrêmes, 91680 Bruyères-le-Châtel, France*
[12]*ELI-Beamlines, Institute of Physics, Czech Academy of Sciences, 25241 Dolní Brezany, Czech Republic*
[13]*CEA-CESTA, CS 60001, 33116 Le Barp Cedex, France*
[14]*LULI-CNRS, CEA, Sorbonne Universites, Ecole Polytechnique, Institut Polytechnique de Paris, F-91128 Palaiseau Cedex, France*
[15]*Department of Electrical and Computer Engineering, University of Alberta, Edmonton, T6G1R1 Alberta, Canada*
[16]*Department of Physics, University of York, Heslington YO10 5DD, United Kingdom*
[17]*Centro de Laseres Pulsados, Building M5, Science Park, 37185 Villamayor, Salamanca, Spain*
[18]*Aix Marseille Université, CNRS, PIIM, F-13013 Marseille, France*
[19]*ETSI Aeronáutica y del Espacio, Universidad Politécnica de Madrid, 28040 Madrid, Spain*
[20]*Department of Physics, University of Nevada, Reno, Nevada 89557, USA*

(Received 1 April 2022; accepted 25 July 2022; published 19 September 2022)

Investigating the potential benefits of the use of magnetic fields in inertial confinement fusion experiments has given rise to experimental platforms like the Magnetized Liner Inertial Fusion approach at the Z-machine (Sandia National Laboratories) or its laser-driven equivalent at OMEGA (Laboratory for Laser Energetics). Implementing these platforms at MegaJoule-scale laser facilities, such as the Laser MegaJoule (LMJ) or the National Ignition Facility (NIF), is crucial to reaching self-sustained nuclear fusion and enlarges the level of magnetization that can be achieved through a higher compression. In this paper, we present a complete design of an experimental platform for magnetized implosions using cylindrical targets at LMJ. A seed magnetic field is generated along the axis of the cylinder using laser-driven coil targets, minimizing debris and increasing diagnostic access compared with pulsed power field generators. We present a comprehensive simulation study of the initial B field generated with these coil targets, as well as two-dimensional extended magnetohydrodynamics simulations showing that a 5 T initial B field is compressed up to 25 kT during the implosion. Under these circumstances, the electrons become magnetized, which severely modifies the plasma conditions at stagnation. In particular, in the hot spot the electron temperature is increased (from 1 keV to 5 keV) while the density is reduced (from 40 g/cm^3 to 7 g/cm^3). We discuss how these changes can be diagnosed using x-ray imaging and spectroscopy, and particle diagnostics. We propose the simultaneous use of two dopants in the fuel (Ar and Kr) to act as spectroscopic tracers. We show that this introduces an *effective spatial resolution* in the plasma which permits an unambiguous observation of the B-field effects. Additionally, we present a plan for future experiments of this kind at LMJ.

DOI: 10.1103/PhysRevE.106.035206

I. INTRODUCTION

Magnetization is a promising strategy to increase fusion yields and relax ignition criteria in laser-driven Inertial

*gabriel.perez.callejo@uva.es
†joao.santos@u-bordeaux.fr

Confinement Fusion (ICF) [1], as the presence of a B field strongly modifies fundamental properties of High Energy Density (HED) plasmas. In ICF implosions, this concerns (among other key mechanisms) heat transport, which governs the transfer of the laser energy from the corona to the ablation front, and becomes anisotropic [2,3] in the presence of a strong B field ($\sim$kT). Seed B fields can be amplified by $\sim$500 times to strengths up to $B > 10\,$kT through compression of the plasma [4]. This increases the fusion yields as it inhibits the thermal energy transport and reduces the loss of α particles from the hot spot perpendicularly to the B field [1,4–6]. Additionally, magnetized implosions may be less vulnerable to hydrodynamic instabilities [7,8] that could lead to disadvantageous mixing of the hot and cold parts of the target [9]. Suppressing these instabilities is a crucial issue to reach ignition at the National Ignition Facility (NIF) [10–12].

A common approach to magnetoinertial fusion is the use of cylindrical geometries with an axial B field, which was originally used in the Z-pinch Magnetized Liner Inertial Fusion (MagLIF) experiments at the Z-machine [13,14]. Profiting from the advantages described above, combined with this favorable geometry, the cylindrical compression is expected to be near adiabatic and stable, with a lower implosion velocity and convergence ratio than in conventional ICF. To explore this approach with a higher repetition rate and easier diagnostic access than on the Z-machine, a laser-driven downscaled MagLIF approach is being explored at the OMEGA 60 laser facility [15], thus facilitating investigations of the underlying physics [16–20]. At OMEGA, the axial seed B field is generated using external capacitive pulsed discharges with the Magnetoinertial Fusion Electrical Discharge System (MIFEDS) [21], which can produce B fields of up to $\sim$30 T.

However, the MIFEDS system blocks the line of sight that follows the axis of the cylinder, which complicates the study of radial gradients and instabilities during the implosion. Additionally, it produces a significant amount of debris that can be damaging to the nearby diagnostics and the facility in general. As an alternative strategy, the generation of B fields using Laser-Driven Coil (LDC) targets has recently begun to be investigated for cylindrical implosion experiments at OMEGA [22,23]. This approach builds upon the demonstration of the compactness and performance of these targets observed in recent laser-plasma experiments carried out within laser facilities of more modest energies [24–28]. Laser-driven B field targets could potentially extend the range of available magnetization levels that can be reached in the imploding plasma. Additionally, contrary to MIFEDS, they are practically debris-free, and do not considerably block the line of sight of diagnostics to the target, thus facilitating the study of the implosion in both axial and radial directions. Independently of the method that is used to generate the seed B field, the extreme magnetization phenomena produced in these cylindrical implosion experiments have been recently studied using extended Magnetohydrodynamics (MHD) simulations [29].

In this context, we present an experimental design for studying the dynamics of imploding plasmas under extreme magnetizations at the Laser MegaJoule (LMJ) facility [30,31].

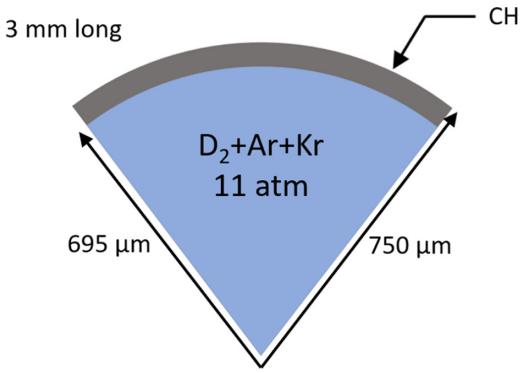

FIG. 1. Schematic design of the cylindrical targets, showing the plastic shell and the gas fuel. This cylinder is 3 mm long and the thickness of the CH shell is 55 μm.

We build on the aforementioned MagLIF experiments at OMEGA 60 using LDCs.

We present results using state-of-the-art MHD, atomic physics, and radiation transport simulation tools, which show that it is possible to reach conditions for extreme magnetizations using a relatively low-seed B field. In particular, a 5 T initial B field can be compressed to $>10\,$kT, thus allowing unique studies of the impact of magnetization on electron heat transport, magnetic flux compression, stagnation temperatures, and fusion reaction yields.

The paper is structured as follows. In Sec. II, the experimental configuration is described, including the restrictions for target dimensions and laser pointing. Section III presents the expected values of the seed B field that can be produced within this design. This is expanded upon in the Appendix, which describes the physical model used to describe the B-field generation using LDCs and details the results and analysis from a recent experiment at OMEGA in which LDCs were characterized in conditions similar to those at LMJ. In Sec. IV, we present the results from extended MHD simulations showing the compression of the seed B field and its effect on the plasma conditions compared to the simulations for the unmagnetized case. Section V discusses a variety of diagnostics to characterize the experiment and, finally, Sec. VI discusses the conclusions and future perspectives of this paper.

II. EXPERIMENTAL CONFIGURATION

The proposed experimental configuration consists of a D_2 - filled plastic cylinder positioned at the Target Chamber Center (TCC), whose axis is aligned with the target chamber vertical axis. The cylinder is 3-mm-long, 750 μm outer radius—55-μm-thick plastic shells (CH, 1.1 g/cm^3) filled with D_2 at 11 atm (1.81 mg/cm^3), as shown in Fig. 1. Targets have been designed to have the minimum size, while ensuring that the focused LMJ laser beams are effectively terminated on target.

We propose the use of a dopant in the gas to regulate the core temperature [29] and, most importantly, to act as a spectroscopic tracer for characterizing the plasma conditions. In particular, we propose using argon, krypton, or rather a combination of the two. Both elements have been previously used as spectroscopic tracers for ICF-related experiments [33–37].

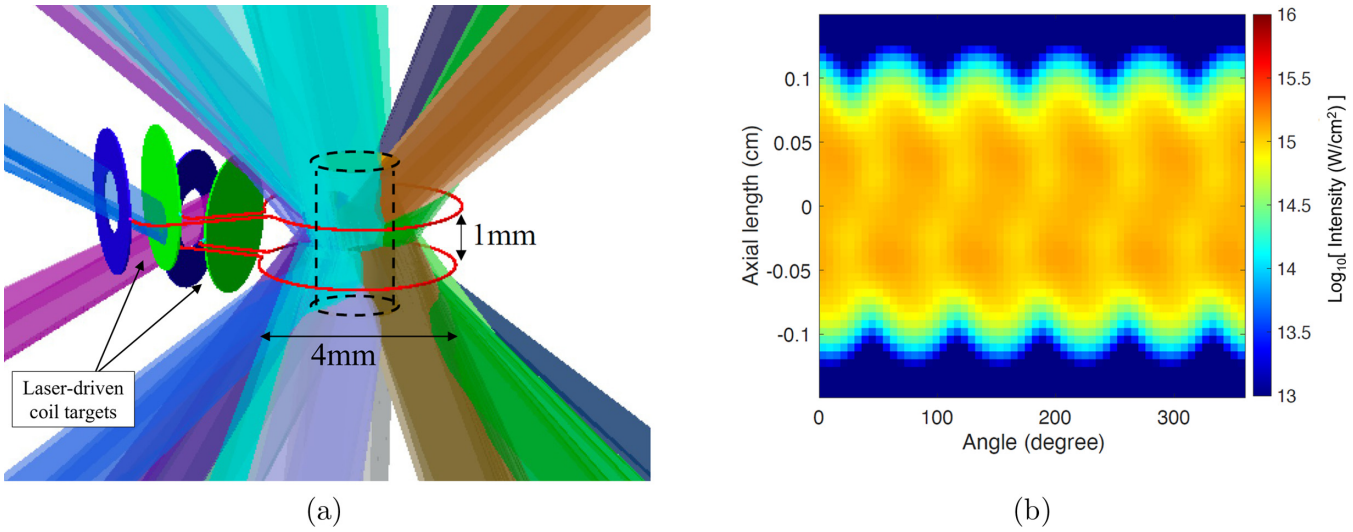

FIG. 2. (a) VisRad [32] image showing the proposed configuration of the targets, with the 80 active laser beams for cylindrical compression. The beams' radius in display corresponds to 99% enclosed beam energy. The cylindrical target position is displayed by a black dashed line contour. Additionally, the figure shows the coil targets, mounted around the cylinder, with a gap distance between coils of 1 mm. In this configuration, the B field generated at the axis of the cylinder is expected to be $\sim 5 - 10$ T. It can be seen how the coil targets are away from the LMJ beams that irradiate the cylinder. (b) Laser intensity on the cylindrical target using the proposed drive configuration. The intensity is $(11.6 \pm 1.2) \times 10^{14}$ W cm^{-2} over the central 1 mm region.

While the dopant concentration will decrease the obtainable temperature owing to radiative losses, the choice of dopant will determine the plasma conditions that can be probed using spectroscopic diagnostics. This is discussed further in Sec. V.

The cylindrical target is imploded using 80 laser beams as shown in the VisRad [32] image in Fig. 2(a). These are grouped into 20 groups (quads), each of which delivers a total energy of 13.5 kJ using a 3 ns square pulse [38] of 3ω light ($\lambda = 351$ nm). The quads are uniformly distributed in four rings around the vertical axis of the chamber, with polar angles 33.2°, 49°, 131°, and 146.8°. This generates an irradiation profile on the cylinder as shown in Fig. 2(b). Over the central region of the target (± 0.5 mm), the drive is reasonably uniform, with an intensity of $(11.6 \pm 1.2) \times 10^{14}$ Wcm^{-2}. This corresponds to a 6% variation in the azimuthal direction and a 4% axial variation.

Around the cylindrical target, two copper coil targets in a quasi-Helmholtz configuration are mounted, as shown in Fig. 2(a). The purpose of these LDCs is to generate a seed B field along the axis of the cylinder [26,27,39–43], and magnetize the central region of the fuel. The coils are positioned at $z = -0.5$ mm and $z = 0.5$ mm, where $z = 0$ corresponds to TCC (thus covering the central 1 mm axial length of the cylinder). The coils' axes are coincident with the cylinder target axis and with the vertical axis of the interaction chamber. Although the exact design of the coil targets (diameter of the plates, wire length, and orientation) can be modified, the diameter of the coils must be large enough so they are not irradiated by the laser beams driving the implosion [in Fig. 2(a), we show the radius of the laser beams that contains 99% of their energy]. We choose a coil diameter of 4 mm, to minimize the target inductance, yielding 13 nH, while keeping clear of the beams.

Recent experiments at the PALS [44] and LULI [45] laser facilities using LDC targets indicate that the shock generated in the irradiated plate takes ~ 1 ns to traverse the thickness of a 50-μm-thick plate (in agreement with hydrodynamic simulations), and that the x-ray radiation emitted from the back of the plate is too weak to pre-heat targets on the other side. Nevertheless, as an additional precaution, to avoid direct x-ray irradiation from these copper plates that could modify the implosion dynamics, in the design presented here the plates of the coil targets are oriented so their surface normal directions do not intersect with the cylindrical target. The side-on emission from the plasma generated between the plates does not intersect with the cylindrical target either. In addition, the thickness of the irradiated plate must be adapted to the laser pulse duration.

The coil targets are driven by two additional 3ω laser quads (one per coil target), delivering a total of 13.5 kJ to each coil target, with a circular focal spot, 375 μm in diameter (at $1/e$ intensity), and a minimum pulse length of 3 ns. This corresponds to a maximum intensity of $\sim 4 \times 10^{15}$ Wcm^{-2} on the coil plates, although the duration of the pulse can be extended to tune the initial B field. These quads are incident at 59.5° and 120.5° from the vertical axis of the chamber, respectively, and separated by an azimuthal angle of 18°.

III. GENERATION OF THE SEED B FIELD

Each of the LDCs consists of two plates, marked in green and blue in Fig. 2(a), connected by a single-loop coil. Laser beams are focused onto the inner plate (green in the figure), thereby ejecting hot electrons toward the outer plate (blue in the figure). This process determines the efficiency of generating a current in the coil and the induced B field.

The underlying physics of LDCs can be described by the plasma *diode* model developed by Tikhonchuk *et al.* [26], where the coil targets are considered as a resistor-inductor (RL) circuit fed by a laser-driven diode current. The laser is

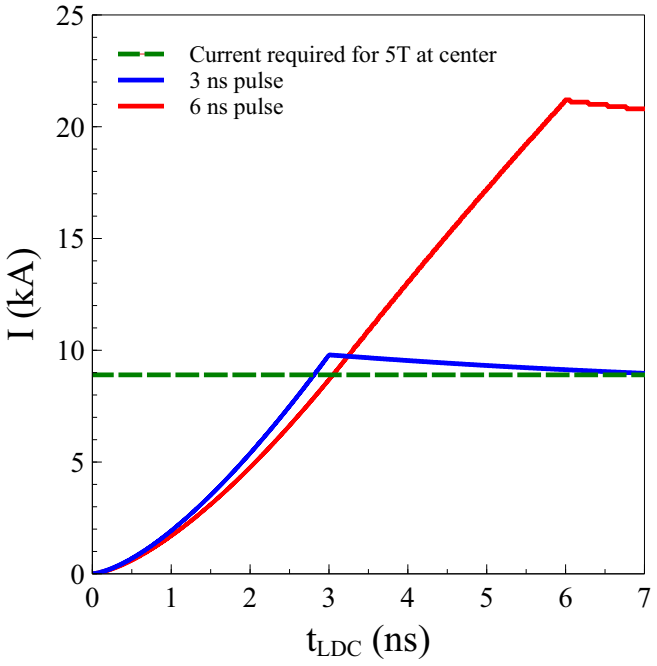

FIG. 3. Time evolution of the current looping through the coil targets for this experiment, depending on the duration of the laser pulse. The timescale corresponds to that of the laser beams driving the LDCs. The main target beams are delayed by 3 and 6 ns, respectively, so the seed B field is maximum prior to their activation.

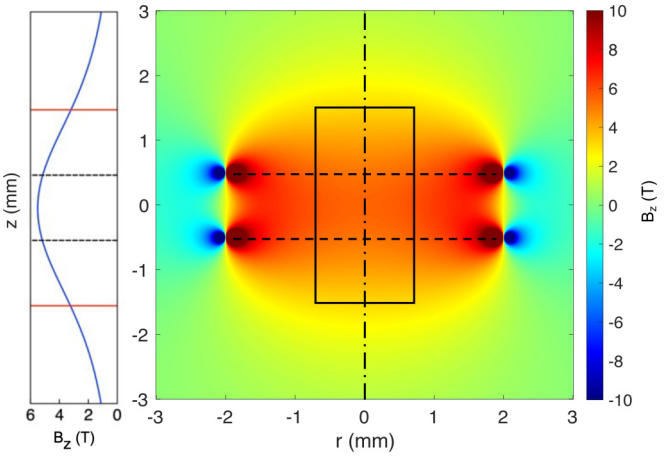

FIG. 4. Two-dimensional distribution of the seed magnetic field across the cylinder. In this figure, the horizontal dashed lines represent the position of the coils, whereas the solid-line rectangle corresponds to a transverse cut of the cylindrical target. The seed magnetic field across the central region of the cylinder is uniform, with a value of ∼5.5 T.

typically of ns duration and sufficiently intense to generate a significant number of nonthermal (hot) electrons. The hot electron temperature is obtained as a function of the laser irradiance $I\lambda^2$, using known scaling laws [26]. With respect to the conversion efficiency of laser energy into hot electrons, values in the literature range from ∼1% [46–50] to ∼10% [51,52]. Here we assume a conversion efficiency of 1%, following the recent results from Zhang *et al.* [50], obtained at the OMEGA facility for 3ω laser interactions with solid foils. Further details on this model and the physics behind the LDCs are given in the Appendix.

For the conditions at LMJ, the predicted hot electron temperatures are 7.5 keV and 6.5 keV, for 3 and 6 ns laser pulse drives, respectively. Correspondingly, we estimate peak currents on the coils of 10 kA and 20 kA. These correspond to a seed B field between 5.5 and ∼10 T at the center of the quasi-Helmholtz system. For the rest of this paper, we will work with a conservative value of 5 T to ensure the feasibility of the platform.

The inductance of the proposed LDCs for LMJ is 13 nH, twice the value of those used at OMEGA (see Appendix). This is a limiting constraint determined by the large spatial scale of the experiment. However, the configuration of the LMJ beams allows us to place the two coils in Helmholtz configuration, as shown in Fig. 2(a), which allows us to amplify the B field over the cylinder volume.

Figure 3 shows the time evolution of the current for the two laser pulse durations mentioned above (3 and 6 ns), together with the current that is required for a 5 T field at the center of the Helmholtz system (8.9 kA). Note that although the peak current is obtained at the end of the laser pulse, owing to the RL-circuit behavior, after the end of the laser the current decreases very slowly, staying relatively constant over several nanoseconds. The beams that drive the cylindrical target are activated at the end of the LDC drive to reach the maximum seed B field before the main target is imploded.

Although the highest B field is obtained for a longer pulse since the characteristic RL time is still longer than the laser drive, it should be noted that the pulse cannot be arbitrarily long, since there are additional physical processes that will limit the current. If the pulse is too long, the generated shock will break out on the opposite side of the driven plate, thus leading to a reduction of the laser-target energy coupling. Additionally, if the plasma between the plates becomes too dense, it may short-circuit the coil. Besides, the laser energy will no longer be deposited in the rear plate.

An example of magnetic field distribution is shown in Fig. 4 for the experimental parameters described in Sec. II, and a pulse length of 3 ns (the figure corresponds to the peak B field obtained at the end of the laser pulse). The solid-lined rectangle corresponds to the cylindrical target, while the horizontal dashed lines represent the position of the coils. A vertical lineout along the cylinder axis (vertical dashed-dotted line) is shown for clarity on the left of the image. The produced B field has an acceptably uniform value of ∼5.5 T over the length of the central region of the target (between the coils). This field corresponds to a wire current of 9.8 kA. Using RADIA [53], the magnetic field can be integrated in a volume around both coil targets to yield a magnetic field energy of

$$\int \frac{B^2}{2\mu_0} dV = 1.4\,\mathrm{J}. \tag{1}$$

This corresponds to a fraction of 5×10^{-5} the total laser drive energy of 27 kJ used to generate the B field.

While the rapid increase of the coil B field could give rise to eddy currents within the target that would oppose the generated seed B field and preheat the target, this platform is

designed to minimize this effect. As mentioned in the previous section, the orientation of the irradiated plates of the LDC targets is such that the x-ray burst that will be generated will not intersect with the target. Additionally, the laser contrast at LMJ ensures that the intensity of the prepulse is below $\sim 10^7\,\mathrm{W/cm^2}$, which is not sufficient to ionize the target and generate a preplasma. For these reasons, the target should remain an insulator during the rise time of the B field, so no currents can be induced, and the B field can soak into the cylinder volume.

IV. IMPLOSION HYDRODYNAMICS

To characterize the plasma evolution and measurable outputs from the experiment here proposed, we have performed two-dimensional extended-MHD simulations using the code Gorgon [9,29,54]. These simulations include radiation transport, magnetized heat transport, Biermann battery, Nernst effects, and updated forms of transport coefficients [55], which have been shown to reduce the level of magnetic field twisting for premagnetized implosion simulations [56]. We have performed simulations both for a nonmagnetized implosion and using a 5 T seed B field, as predicted by the model in Sec. III (see Fig. 4).

In these simulations, a 0.3% atomic percentage of Ar has been added to fulfill the role of the spectroscopic tracer mentioned in Sec. II. The addition of this dopant will lower the overall temperature of the implosion, owing to radiative cooling. This effect will depend on the initial magnetic field and the dopant percentage, as discussed in depth in our previous paper [29].

The laser-target configuration described in this paper is prone to the cross-beam energy transfer (CBET) parametric instability due to the counterpropagating beams crossing in a large volume and the high intensities involved. To account for this effect, the MHD simulations presented here include an artificial reduction of the laser energy of 30%. To check this estimation of the CBET effect, the temperature and density maps obtained from the hydrodynamic simulations were studied with the code IFRIIT [57], including quad-by-quad interaction in the full three-dimensional configuration at different stages of the implosion. We found high CBET gains, with reduction in the laser-target coupling up to $\sim 30-40\%$, which validates our first estimate.

From Fig. 2(b), it can be seen that the laser irradiation pattern presents some modulations (4% axially and 6% azimuthally) which could be amplified by CBET as well. However, the amplification of low-mode modulations by CBET is a second-order effect, with a much lower impact on implosion performance than the reduction of the laser drive itself. Furthermore, recent work on scaling cylindrical implosions to indirect drive facilities has shown how low-mode instabilities can be minimized [58,59], thus reducing the effect of CBET-induced growth. For these reasons, we do not expect CBET amplification of the laser imprint modulations to significantly impact our implosion estimates further than the $30-40\%$ reduction mentioned above. Nevertheless, at the moment, there are three diagnostics at LMJ that can characterize the effects of CBET and further laser-plasma instability experiments are currently undergoing, so prior to fielding this platform, these estimates will be updated.

In addition to CBET, we expect the laser coupling to be reduced further owing to scattered light from stimulated Raman scattering (SRS). Nevertheless, the hot electrons generated by this process ($\sim 30-50\,\mathrm{keV}$) are not likely to be detrimental to the implosion performance, since the areal density of the imploding cylinder ($\langle \rho R \rangle \sim 7-10\,\mathrm{mg/cm^2}$) can effectively stop electrons with energies $<70\,\mathrm{keV}$ from reaching the core. It is possible that more energetic electrons are generated via the two-plasmon decay mechanism (up to $\sim 100\,\mathrm{keV}$) or by SRS in laser filaments, which could eventually preheat the fuel, thus reducing the efficiency of the compression. However, SRS is the dominant mechanism in the long scale-length plasmas expected in our conditions, and the laser intensity is not high enough to lead to significant filamentation and the associated production of high-energy hot electrons through SRS [60].

Stagnation occurs at 3.5 ns after the start of the main drive in both the unmagnetized case and with a 5 T seed B field. Note that this timescale is different from that shown in Fig. 3, since the LDCs are driven prior to the cylindrical target. Further to this, Fig. 3 shows that, after the maximum current is reached, the current stays relatively constant ($\pm 10\%$) for the 3.5 ns required to reach stagnation. The results at stagnation time are shown in Fig. 5. In this figure, the left-side images correspond to 2D maps of the predicted conditions, while the right-side column shows radial lineouts through the center of the cylinder. In the two-dimensional image, the temperature (right) and density (left) of an unmagnetized (bottom half) and a magnetized (top half) implosion are compared; whereas the images with the lineouts show the radial distribution of the compressed B field at stagnation and the mass density at the top, and the electron temperature at the bottom for both the magnetized and the unmagnetized cases. The dotted vertical lines indicate the core boundary for both cases.

It can be seen how, in the magnetized case, the core is heated up to $>5\,\mathrm{keV}$, compared to ~ 1 keV in the unmagnetized case. On the other hand, when a magnetic field is applied, the density at the center of the core is $7\,\mathrm{g/cm^3}$, while in the unmagnetized case it is compressed up to $40\,\mathrm{g/cm^3}$. The former is owed to the fact that the thermal energy losses are reduced by magnetizing the electrons; while the latter is a consequence of the increased magnetic pressure in the core, as well as the fact that the thermal pressure is increased in a hotter plasma ($P \propto \rho T$). Additionally, the initial B field of 5 T is compressed up to 25 kT across the core of the target. This corresponds to an amplification of the seed B field by a factor ~ 5000, while the fuel is compressed by a factor of $(R_0/R)^2 \sim 10^4$. Note that the B field seems to be almost *frozen* in the plasma flow (the magnetic flux is conserved throughout the implosion). This is not an approximation made in the simulations but rather a direct consequence of the fact that the plasma compresses the B field faster than it can diffuse away. This is characterized by a high value of the *magnetic Reynolds number*, which is defined as

$$R_M = \frac{UR}{\eta}, \tag{2}$$

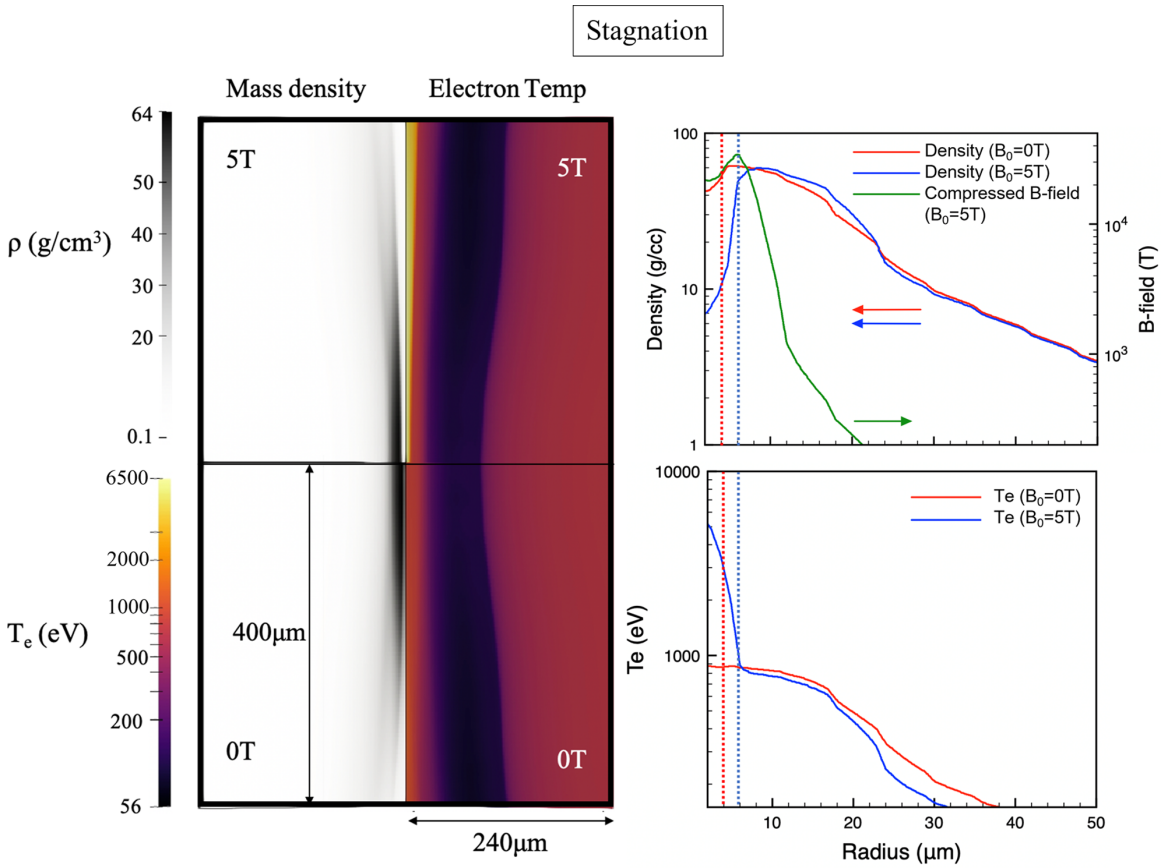

FIG. 5. Left panel: Two-dimensional $r-z$ Gorgon simulations showing the density (left side) and temperature (right side) maps at stagnation (3.5 ns after the start of the main drive) for the case with a 5 T seed B field (top) and the unmagnetized case (bottom). Right panel: Radial lineouts through the center of the cylinder, of the density, electron temperature, and compressed B field at stagnation for magnetized (blue) and unmagnetized (red) implosions. The dotted vertical lines indicate the core boundary for both cases. These simulations include radiation transport and Biermann battery effects, along with Nernst and Hall transport.

where U is the implosion velocity and R is the plasma radius at a given time and η is the magnetic diffusivity. From our MHD simulations we calculate $R_M \sim 200$.

To quantify the effect of the magnetic field on the plasma, we use the following metrics [29]:

$$\beta = \frac{P_{\text{thermal}}}{P_{\text{magnetic}}}, \tag{3}$$

$$\chi_e = \omega_e \tau_e, \tag{4}$$

where P_{thermal} and P_{magnetic} are the thermal and magnetic pressures, respectively, ω_e is the electron cyclotron frequency (eB/m_e), and τ_e is the characteristic timescale of electron-ion collisions ($\propto T_e^{3/2}/n_e$, where T_e and n_e are the electron temperature and density, respectively). With these definitions, the β parameter indicates the relative significance of the magnetic field for the macroscopic plasma motion (a value of $\beta \lesssim 100$ already means that the magnetic pressure plays a significant role), whereas χ_e (the so-called *Hall parameter*) gives an indication of the role of the B field on the electron energy transport (a low χ_e means low magnetization).

The obtained simulation results in the stagnated core correspond to $\beta \sim 9$ and $\chi_e \sim 40$. This means that the magnetic pressure in the core of the plasma is one-ninth of the thermal pressure, and an electron, on average, does ~40 rotations around the magnetic field line before colliding with an ion. This indicates that a 5 T seed B field is enough to significantly magnetize the implosion, altering electron transport (less energy losses perpendicular to the B field) and pressure balance, thus modifying the hydrodynamic conditions of the implosion, and of the plasma at stagnation.

The high value of χ_e indicates that the electrons become magnetized, with Larmor radius smaller than the mean-free path. This reduces the energy transport rate due to electron-ion collisions, which can increase electron temperature significantly above the ion temperature. This has two important effects. First, the heat conduction becomes anisotropic since it now occurs preferentially along the electrons' magnetic orbits. This anisotropy not only modifies the temperature profile (as seen in Fig. 5), but also the heat wave propagation, localizing the hot plasma in regions of stronger B field. Second, nonlocal effects (such as the depletion of the high-energy tail of the electron distribution) are reduced perpendicular to the magnetic field. In addition, large azimuthal currents can be induced, which transport magnetic and thermal energy. The magnetic energy is converted into electron energy through resistive diffusion and Ohmic heating. As an example consequence, the large values of the Hall term indicate that the B field itself can be twisted azimuthally owing to these induced currents. Therefore, the experimental platform described here

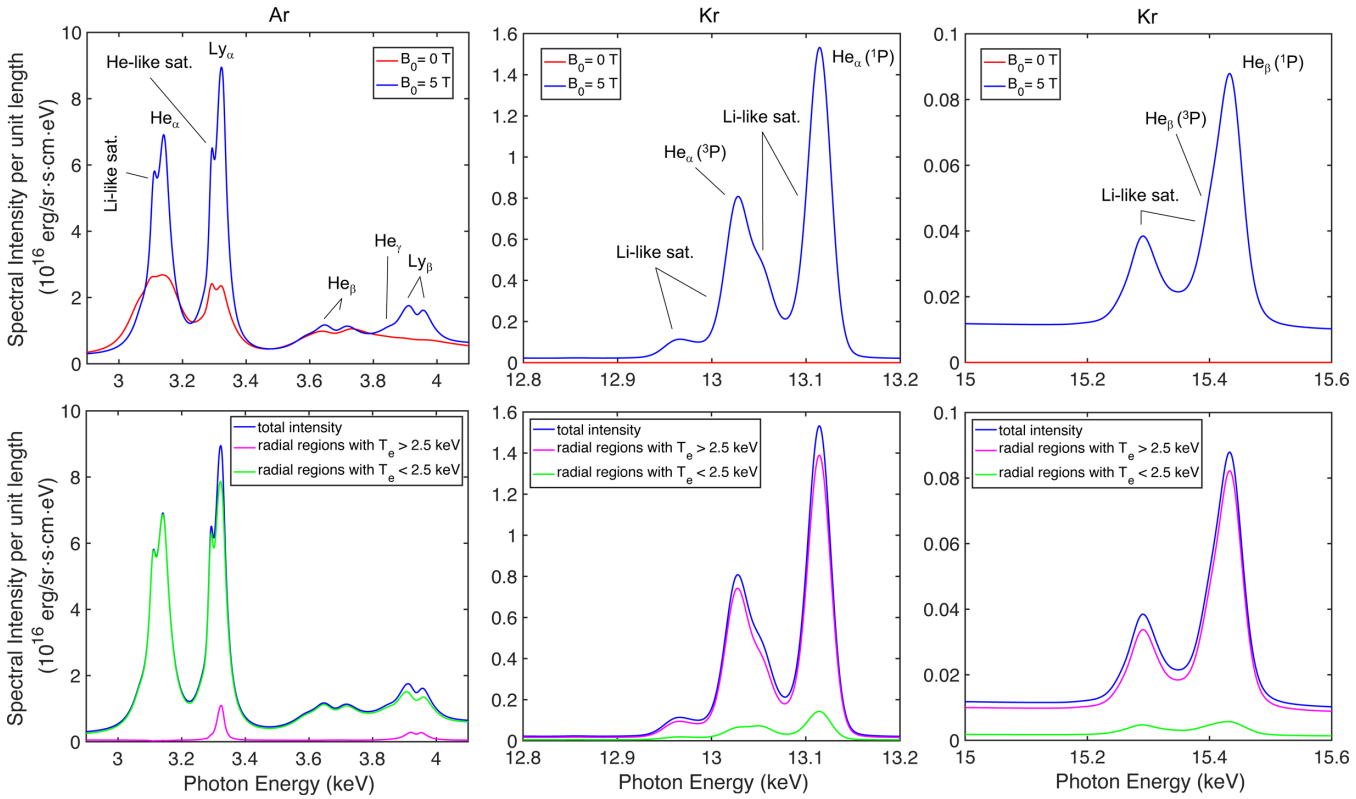

FIG. 6. Top row: Ar (left) and Kr (middle and right) K-shell emission spectra at stagnation, for both a nonmagnetized (red) and a magnetized (blue) case. For the Kr case, the middle figure shows the He_α emission region while the right figure shows the He_β lines. These spectra have been obtained using a cylindrical radiation transport model, using the radial profiles of the plasma conditions predicted by Gorgon (as shown in Fig. 5). Bottom row: Ar (left) and Kr (middle and right) K-shell emission spectra at stagnation for the magnetized case. The blue line corresponds to the total intensity, whereas the green and purple lines correspond to the contributions from regions of the plasma at temperatures below and above 2.5 keV, respectively. This shows that each element probes different regions of the core, introducing an effective spatial resolution. The spectra include contributions from Stark and Doppler broadening, as well as the instrumental broadening corresponding to the resolution achievable at LMJ ($E/\Delta E \sim 500$).

opens the path to observing and characterizing these effects, which is fundamental to understand this extreme magnetization regime [29].

V. EXTRACTION OF PLASMA PARAMETERS THROUGHOUT THE COMPRESSION

A main goal of the proposed experimental platform is to probe the changes on the hydrodynamic conditions of the imploding core due to the impact of the compressed magnetic field. This can be observed by means of a spectroscopic tracer. For instance, Ar doping of ICF implosions is commonly used to extract the density and temperature conditions of imploding cores [34,35,61–63]. This technique exploits two basic properties of the Ar K-shell spectrum emitted from hot and dense plasmas: (1) the strong dependence on density of the Stark-broadened line shapes and (2) the dependence (through the atomic population kinetics) of the relative intensity distribution of K-shell lines and associated satellite transitions on electron density and temperature. The Ar K-shell emission is, however, sensitive to temperatures between $\sim$600−2500 eV and, therefore, for an application to a hotter scenario, a higher-Z spectroscopic tracer, such as Kr, suits better.

Given the large variations expected for the core conditions in the magnetized case (see Fig. 5), to probe the conditions at the different regions of the compressed core, we propose the use of a combination of Ar and Kr doping in the deuterium plasma.

As illustration, the top row of Fig. 6 shows Ar and Kr K-shell synthetic spectra for the conditions at stagnation for both a nonmagnetized (red) and a magnetized (blue) case. Owing to the range of energies that these spectra cover, the Ar K-shell emission (including $n = 2 \rightarrow 1$, $3 \rightarrow 1$ and $4 \rightarrow 1$ line transitions in He-like and H-like Ar) is shown on the left, and the Kr He_α ($n = 2 \rightarrow 1$) and He_β ($n = 3 \rightarrow 1$) photon energy regions are shown on the middle and right, respectively. Consistently with the Gorgon MHD simulations, an Ar atomic concentration of 0.3% in the deuterium plasma was used. Additionally, based on the study conducted in previous works [29,36] and to keep a low impact of Kr radiative losses on the hydrodynamics, a 0.01% of Kr was considered. We note in passing that groups of $n = 4 \rightarrow 2$ line transitions in Kr ions—from Be-like to He-like—also might arise in the Ar K-shell photon energy range shown in Fig. 6. However, mainly due to the difference on the concentrations, the referred Kr emission becomes negligible compared to the Ar one.

These spectra were obtained by solving the radiation transport problem in cylindrical geometry for the radial profiles of temperature and density predicted by Gorgon, as indicated in Fig. 5. Line of sight was assumed to be perpendicular to the cylinder axis. The required frequency-resolved emissivities and opacities (including bound-bound, bound-free, and free-free contributions) and atomic-level population distributions were calculated using the collisional-radiative model ABAKO [64]. In particular, for this application we used an updated version for multicomponent plasmas. Thus, for given temperature and density values of the plasma mixture, the population kinetics of the Ar and Kr tracers are solved self-consistently, with both species sharing a common free electron pool arising from the ionized deuterium plasma and their own converged ionization balance [65]. The attenuation of the core emission through the compressed shell was not explicitly taken into account in the radiation transport calculations presented here. Optical depth estimations for the plastic shell at stagnation conditions in the Ar *K*-shell photon energy range suggest that a correction to account for the attenuation by the shell—as described in Ref. [35]—might be needed to properly analyze the spectra and extract the core temperature values. The impact of this effect is expected to be minimum for the higher photon energy range corresponding to the Kr *K*-shell spectrum. In any case, our estimates indicate that it will be feasible to observe the tracers' spectra. Moreover, previous experiments at the NIF [36,37] have observed Kr line emission in similar conditions using 64-μm-thick plastic shells.

Importantly for this spectroscopic application, in an attempt to obtain a faithful representation of the emergent spectrum, reliable and detailed Stark-broadened line profiles of the most prominent transitions are needed when performing the radiation transport calculations. In this regard, the Stark line shapes for the shown parent transitions in Ar and Kr—i.e., He_α, He_β, and He_γ, Ly_α and Ly_β in Ar; and He_α and He_β in Kr—were obtained by the computer simulation code SIMULA [66]. In this code, the plasma is described as a collection of independent particles trapped in a spherical box and the statistics of relative velocities of the emitters and the perturbing ions are obtained using the so-called μ-*ion model* [67]. Calculations are then done using the *no-quenching* approximation, i.e., field mixing between the upper (initial) and lower (final) states was neglected due to the large energy separation between them. Furthermore, Stark line profiles of the associated satellite transitions with spectator electron in $n = 2$ and $n = 3$ were also calculated. For satellite transitions, the calculation by the computer simulation technique becomes prohibitive due to the high number of energy states that must be taken into account and, therefore, the required line-shape database was obtained using a recently developed model that follows the framework of the Stark-broadening standard theory [68] and employs an optimized version of the formalism and numerical methods described in Ref. [69]. We checked that results from this line shape code agree within >99% with those obtained using computer simulations with static ions for some selected and affordable cases of interest. It is worth noting that the Zeeman splitting of the lines cannot be used to directly determine the compressed B field through spectroscopic observation, since in these conditions the Stark broadening is significantly larger (as the electron density reaches values $\sim 10^{25}\,\mathrm{cm}^{-3}$) and blurs the Zeeman pattern [27]. Besides the Stark-broadening mechanism, the spectra shown in Fig. 6 also include Doppler and instrumental broadening. For the latter, we applied a Gaussian convolution consistent with the spectral resolution achievable at LMJ ($E/\Delta E \sim 500$).

From Fig. 6, it can be seen how the krypton acts like a temperature gauge. From this temperature increase, the properties of the B field may be inferred, since no Kr *K*-shell emission is observed in the nonmagnetized case. Note that although the Ar emission is still present in the magnetized case, the relative line intensities and shapes are different from the non-magnetized case (e.g., the Ar Ly_β line emission is only noticeable in the magnetized case). This is owed to the fact that, while in the nonmagnetized case the Ar emission is coming from a roughly uniform plasma at ~1 keV, in the magnetized case, the Ar emission is probing a nonuniform plasma, with temperatures up to ~2.5 keV (above this value the Ar line emission becomes weak). These changes in the line intensity distribution can be used to extract the differences in temperature and density when the core is magnetized.

The bottom row of Fig. 6 focuses on the magnetized case and shows the *effective spatial resolution* that is obtained when using both Ar and Kr as fuel dopants. Most of the emission from Ar comes from regions of the plasma with electron temperatures below 2.5 keV (green lines), whereas in the Kr spectra, the main contributions are those from regions with temperatures above this value (purple lines). Therefore, by looking at the corresponding spatial profiles of core conditions at stagnation, it is clear that while the Ar dopant provides information about the core periphery, the Kr emission allows us to gain insight into the conditions at the core center when the fuel is magnetized.

Owing to the capabilities of the currently available spectrometers at LMJ, the emission spectra can be obtained at different times throughout the implosion, providing a temporal map of the temperature and density of the plasma, as described above. If the magnetic field is assumed to be frozen into the plasma motion (which was shown in Sec. IV to be a good approximation) the temperature and density values can be used to estimate a variety of nondimensional metrics to ultimately determine the relative importance of different mechanisms throughout the implosion collapse [29].

Additional information can be extracted from the neutron emission from the imploded plasma. According to Gorgon 2D simulations, a 25-fold increase in the neutron yield from the hot spot is expected for an implosion with a 5 T seed B field compared to a nonmagnetized implosion ($\sim 5 \times 10^{11}$ and $\sim 2 \times 10^{10}$ neutrons, respectively). This yield can easily be detected by the neutronic detectors already available at LMJ (where the threshold for neutron detection is $\sim 10^8$) [70], providing an additional signature of the B-field effects on the implosion.

The implosion velocity and stability can be diagnosed with x-ray framing cameras that collect the self-emission from the imploding targets [19]. In LMJ, this can be done with both an axial and radial line of sight, with time resolutions of 110 and 130 ps, and spatial resolutions of 35 and 15 μm, respectively [71]. Additionally, the PETAL beam [72] can be used to irradiate a Cu wire to generate an x-ray backlighter and

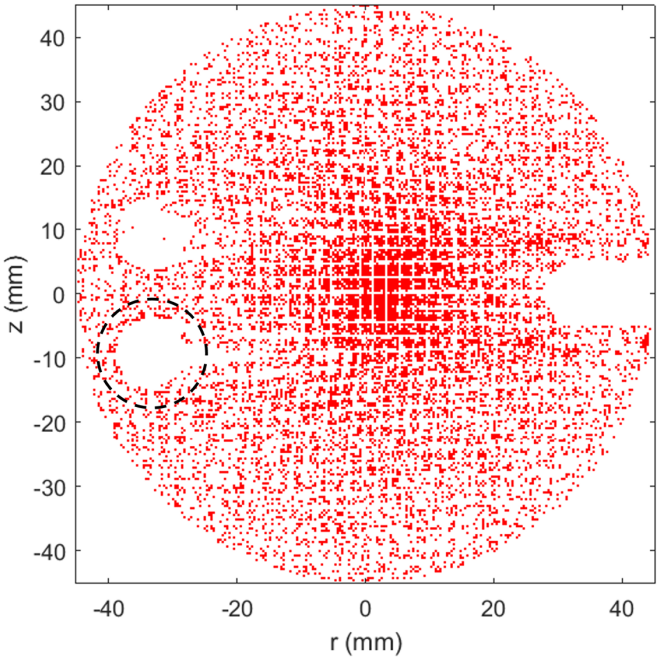

FIG. 7. Synthetic proton radiography image obtained with the particle-tracing code PAFIN [79] for 14.7 MeV protons, using the detector geometry available at LMJ. In particular, the feature that can be observed at the right of the image around $z = 0$ corresponds to the radiochromic film (RCF) holder. The magnetic field produced by each coil leaves a characteristic bulblike feature on the image, and distorts the imprint of the reference mesh (a dashed black circle has been added to point out one of these bulbs). The spatial scale units on the figure correspond to those measured at the detector, so the coils' dimensions are magnified by a factor of $M_c = 16$ ensuing proton probing point projection.

observe the radial profile of the target through x-ray radiography. This is a common technique used in indirect-drive ICF to diagnose the stability and symmetry of the implosion [73,74].

Finally, diagnosing the seed magnetic field is crucial for understanding the conditions of the experiment. For this purpose, we propose the use of proton deflectometry, in a shot with no gas cylinder (only coil targets), using the PETAL beam [72] to produce and accelerate protons up to 51 MeV, via the target normal sheath acceleration mechanism [75]. By placing a reference mesh in the protons' path and recording the imprint of the beam after it traverses the region between the coils, it is possible to obtain an *image* of the deflections caused by the electric and magnetic fields around the coil targets. Although axial probing of the coil targets (that is, sending the protons along the axis of the coils) has been discussed as an accurate method to characterize the generated B field [42,76], owing to the large size and inductance of the targets presented here, the B field signatures that would appear in on-axis radiography are indiscernible with the resolution available at LMJ [77]. For this reason, we propose probing the targets perpendicular to their axes [27,76,78].

Figure 7 shows a synthetic example image of the expected proton radiography results, obtained with the code PAFIN [79] for 14.7 MeV protons. In this case, the proton source is 10 mm away from TCC, the reference mesh has a periodicity of 600 lines/inch and is placed at 3 mm from the source. The detector is placed at 150 mm from TCC, which results in a system magnification of the coil region of $M_c = 16$, while the mesh magnification is $M_m \sim 53$. Additionally, the geometry of the radiochromic film (RCF) proton detectors at LMJ has been used. This can be seen as the 95-mm-diameter circular mask and the white feature at $r \sim 40$ mm, $z \sim 0$ mm (which corresponds to the position of the RCF holder). To produce this figure, a current of 9.8 kA looping through the coils is assumed, which corresponds to the peak current obtained with the model introduced in Sec. III and detailed in the Appendix, for a 3 ns square pulse with an intensity of 4×10^{15} W cm^{-2} (as described in Sec. II). The electrostatic charge accumulated in the targets can be estimated to be of the order of few nC. Given the size of the laser-driven coil targets presented here, the resulting charge density is sufficiently low so electrostatic effects cannot be discerned in the proton radiography images. It can be seen how there is a clear imprint of the magnetic field around the coils on the proton image (this is magnified to $z = \pm 8$ mm on the detector, which corresponds to $z = \pm 0.5$ mm on target). In particular, we have marked with a dashed black circle a characteristic bulblike void feature, which is indicative of a B field sufficiently strong to deflect all protons around that region. Its dimensions can be used to quantify the B field generated by the coil discharge current.

VI. CONCLUSIONS AND FUTURE WORK

We have presented an experimental platform design for studying magnetized cylindrical implosions at LMJ. We propose the use of laser-driven coil targets to generate an initial 5 T B field along the axis of the cylinder. Eighty of the LMJ beams will be used to compress the cylindrical target, while eight additional beams will be used to generate the B field.

The laser-driven coil targets have been modeled following the *diode* model by Tikhonchuk *et al.* [26], suggesting that a fairly uniform seed B field of $\sim 5-12$ T can be achieved over the central 1 mm region of the cylinder. This magnetic field can be experimentally diagnosed by means of proton radiography using the PETAL laser.

We have presented a hydrodynamic analysis of the conditions achievable during the implosion and how they are modified by the magnetic field, as it gets compressed with the target. It has been shown that the initial B field value can be compressed up to >10 kT, in a manner which is consistent with the magnetic field being *frozen* in the plasma flow, as a consequence of the high magnetic Reynolds number. Extended-MHD simulations show that the temperature and density of the plasma at stagnation are heavily affected by the presence of the magnetic field. By doping the fuel, the effects of the magnetic field can then be detected using x-ray spectroscopy.

Besides x-ray spectroscopy, we have proposed a set of diagnostics and their setup to characterize the evolution of the implosions and the evolution of the magnetic field. This setup can be directly implemented in the LMJ facility without the need for further development.

Future work includes improving both the performance and understanding of the coil targets, particularly for the poorly explored parameters of the LMJ laser drive (i.e., ~ 10 kJ at

3ω). We expect to benchmark the scaling laws used to estimate the hot electron generation from the laser-target interaction at different laser intensities and particularly for 3ω light. Parallel experimental efforts using lasers of more modest energies are currently being made toward simultaneously measuring the plasma density and the self-generated B fields close to the irradiated plate to characterize the currents that appear in the plasma. Measuring the target stalk leakage current as well as the plasma impedance between the plates will also help us to understand the operation of the targets and the time limitations before shorting the coil circuit. Furthermore, recent advances in x-ray characterization techniques will allow for experimental probing of the wire surface plasma sheath, resolving the spatial distribution and time evolution of the current.

A comprehensive study of CBET mitigation techniques will be performed. It is expected that using lower intensity, longer drive pulses with the same energy, and adapting the targets to achieve similar compression ratios might significantly reduce the CBET impact on the laser-target coupling.

Prior to LMJ experiments, the analysis of recent similar experiments at OMEGA will be used to benchmark the hydrodynamic simulations and study the relative weights of different transport mechanisms prior to these experiments to produce more accurate predictions.

As mentioned in the Introduction, one of the points of interest of applying a magnetic field is the confinement of α particles within the core. While not the purpose of this platform directly (and not yet possible at LMJ), implosions using DT fuel might as well be investigated. For the values presented in this paper, the Larmor radius of the α particles would be larger than the compressed core, resulting in not a significant radial confinement. However, α particles would still be confined along the axis of the cylinder, similarly as in MagLIF experiments, given that their mean-free path is smaller than the length of the cylinder. An estimate of this axial confinement is given by the aspect ratio of the compressed core (R/L, radius over length). Following the results presented in this paper, we can estimate a loss fraction of $\sim$1.3% for the α particles along the axis of the cylinder, which is comparable with MagLIF experiments, where this ratio is of the order of 1% [80]. Further in the future, LMJ is expected to reach energies above 1 MJ. In this case, it will be possible to drive larger targets, yielding a core radius at stagnation larger than the Larmor radius of α particles for a convergence ratio similar to the presented setup.

The results from these experiments will help benchmark the different electron transport and B-field advection and diffusion models used in MHD codes, thus leading to a more accurate understanding of the different mechanisms affecting the hydrodynamic evolution of highly magnetized HED plasmas.

ACKNOWLEDGMENTS

G.P.-C. acknowledges funding from the French Agence Nationale de la Recherche (No. ANR-10-IDEX-03-02 and No. ANR-15-CE30-0011), the Conseil Règional Aquitaine (INTALAX), and the Spanish Ministry of Science and Innovation through the *Margarita Salas* funding program. C.V. and V.O.-B. acknowledge support from the LIGHT S&T Graduate Program (PIA3 Investment for the Future Program, No. ANR-17-EURE-0027). F.S.-V. acknowledges funding from The Royal Society (UK) through a University Research Fellowship. This study has received financial support from the French State in the framework of the Investments for the Future programme IdEx Université de Bordeaux/GPR LIGHT. This material is based upon work supported by the DOE Office of Science Grant No. DE-SC0022250. The work has also been supported by Research Grant No. CEI2020-FEI02 from the Consejería de Economía, Industria, Comercio y Conocimiento del Gobierno de Canarias and by Research Grant No. PID2019-108764RB-I00 from the Spanish Ministry of Science and Innovation.

This work has been carried out within the framework of the EUROfusion Consortium, funded by the European Union via the Euratom Research and Training Programme (Grant Agreements No. 633053 and No. 101052200—EUROfusion). Views and opinions expressed are, however, those of the author(s) only and do not necessarily reflect those of the European Union or the European Commission. Neither the European Union nor the European Commission can be held responsible for them. The involved teams have operated within the framework of the Enabling Research Projects No. AWP17-ENR-IFE-CEA-02, "Towards a universal Stark-Zeeman code for spectroscopic diagnostics and for integration in transport codes," and No. AWP21-ENR-IFE.01.CEA, "Advancing shock ignition for direct-drive inertial fusion."

This work was performed under the auspices of the U.S. Department of Energy by Lawrence Livermore National Laboratory under Contract No. DE-AC52-07NA27344. This document was prepared as an account of work sponsored by an agency of the United States government. Neither the United States government nor Lawrence Livermore National Security, LLC, nor any of their employees makes any warranty, expressed or implied, or assumes any legal liability or responsibility for the accuracy, completeness, or usefulness of any information, apparatus, product, or process disclosed, or represents that its use would not infringe privately owned rights. Reference herein to any specific commercial product, process, or service by trade name, trademark, manufacturer, or otherwise does not necessarily constitute or imply its endorsement, recommendation, or favoring by the United States government or Lawrence Livermore National Security, LLC. The views and opinions of authors expressed herein do not necessarily state or reflect those of the United States government or Lawrence Livermore National Security, LLC, and shall not be used for advertising or product endorsement purposes.

APPENDIX: MODELING AND BENCHMARKING THE B-FIELD GENERATION IN LDCs

When a LDC target is irradiated by a focused laser beam, initially, a plasma is generated close to the surface of the irradiated plate. While this plasma has not reached the second plate, the vacuum electron current between the plates is space-charge limited by the charge that builds up on each plate. When the expanding quasineutral plasma reaches the outer plate, which depends on the plasma fast ion velocity, the charge within the plasma is compensated and the

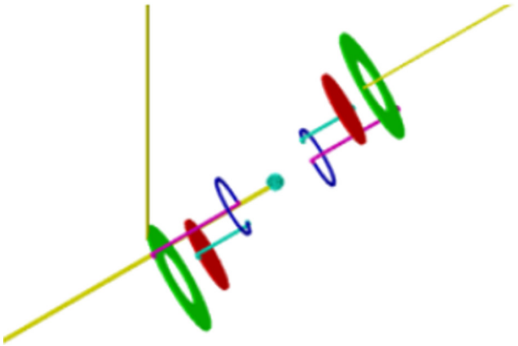

FIG. 8. Schematic design of the experimental setup used at OMEGA, showing the LDCs and the D^3He sphere (light blue in the figure), as seen from the CR39 detector.

potential well close to the interaction plate is strongly reduced. Hot-electron ejection is facilitated and super-Alfvenic ejection currents can be established as the plasma supports a counterpropagating return current. In addition to the space-charge limit, the forward-going current will generate an azimuthal magnetic field that will pinch the plasma between the plates. This magnetization limit depends, among other variables, on the temperature and number of hot electrons.

These two limitations determine the I-V characteristic of the RL circuit [26,81] and, unless the characteristic time $\tau \sim L/R$ (with R and L the circuit resistance and inductance) is reached before the end of the laser pulse, the looping current can increase while the laser keeps irradiating the plate and feeding the system with hot electrons.

The current evolution, $I(t)$, can be computed by solving the following equation:

$$V = L\frac{dI}{dt} + [Z_d + R(t)]I, \tag{A1}$$

where V is the diode potential, Z_d is the plasma impedance between the plates (which accounts for both the space-charge

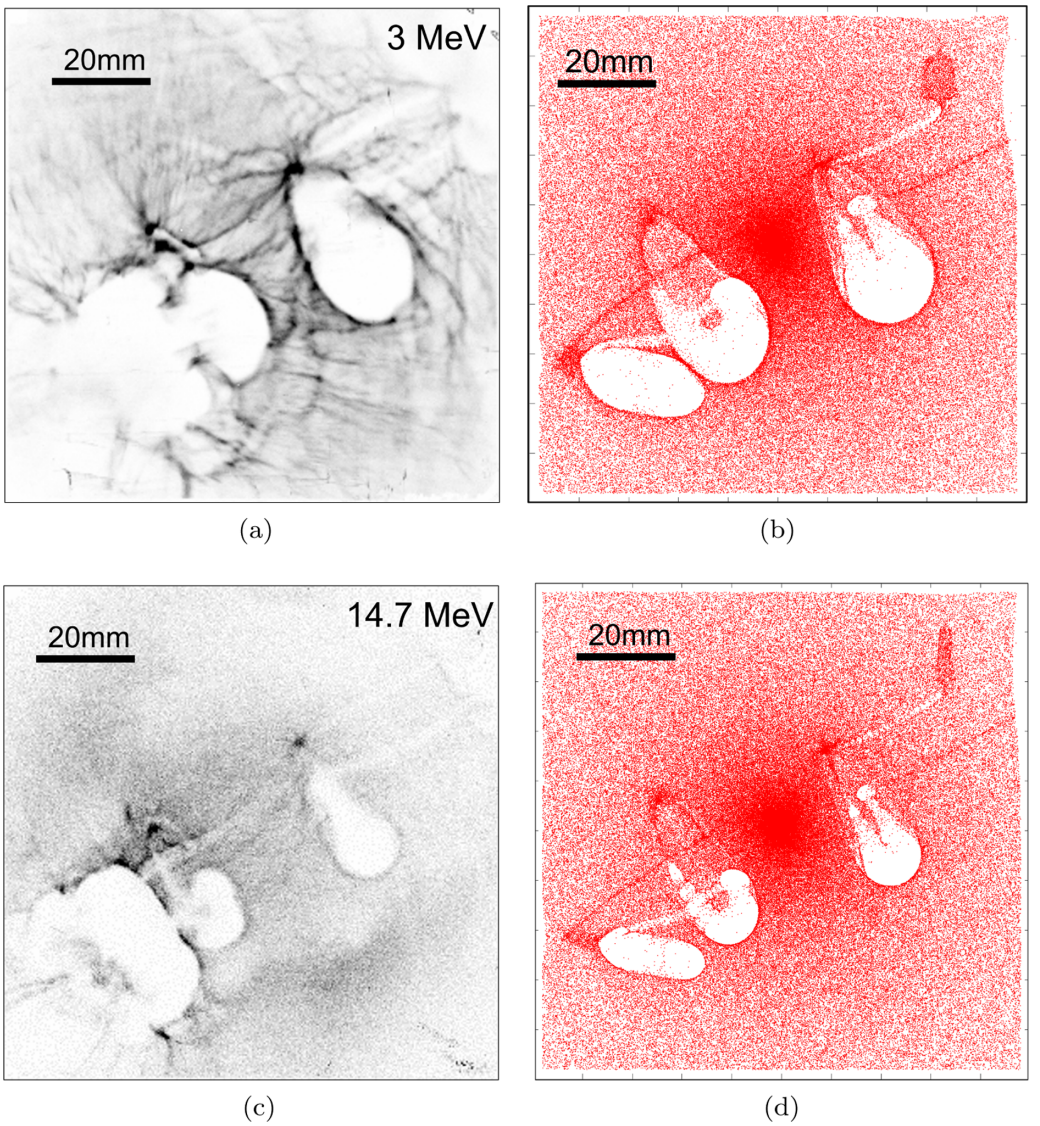

FIG. 9. (a), (c) Example of the obtained proton deflectometry images for 3 MeV and 14.7 MeV protons, respectively. (b), (d) Corresponding synthetic radiographs produced with the code PAFIN. These synthetic images include currents looping through the targets of 6.5 kA and 8 kA, respectively, as well as additional static toroidal charge distributions around the coils of +4.5 nC and +8 nC, respectively.

TABLE I. Results obtained at OMEGA for the two different proton energies, compared with the predictions from the diode model. The last column includes the minimum and maximum currents predicted within the time uncertainty of the measurements.

Proton energy (MeV)	Time (ns)	Measured current (kA)	Predicted current (min.–max. in kA)
14.7	1.50 ± 0.15	8 ± 2	(10.8–11.9)
3	1.73 ± 0.15	6.5 ± 2	(11.4–11.8)

and magnetization limits of the plasma diode), and $R(t)$ is the resistance of the external circuit (the coil wire). Most of the system's dynamics are accounted for by the transient resistance in Eq. (A1), which evolves following the I-V characteristic, as a function of the wire temperature. The inductance stays relatively constant for the duration of the laser pulse, given the low expansion velocity of the wire (of the order of $10\,\mu$m/ns, as measured by Santos *et al.* [27]).

Once the current evolution $I(t)$ has been calculated, the 3D spatial distribution of the B field at any time t_0 can be computed for $I(t_0)$ using a magnetostatic code, e.g., RADIA [53], to which the detailed three-dimensional design of the entire LDC has been previously imported.

There are various physical mechanisms associated with our laser-driven coil platform which cannot be accounted for using such an heuristic plasma-diode model of magnetic field generation. Complications may arise from dense plasma that bridges the target plates and short-circuits the coil, driving the outer plate by prompt x-ray emission from the interaction region, early destruction of the drive plate or deposition of the laser energy in the blow-off plasma before it reaches the solid target. Maintaining a static current and B field over the course of a $\sim$3 ns laser-irradiation time must therefore be seen as a source of risk in these multi-kJ experiments, but previous results on the OMEGA laser, obtained in conditions similar to those at LMJ, give us grounds for optimism.

At OMEGA, we fielded a similar configuration to the one proposed in this paper for LMJ, using a pair of LDCs with 750-μm-radius parallel coils, separated by 2.5 mm (this geometry was constrained by the geometry of the OMEGA beams). The inductance of each of the targets was 6.5 nH.

Magnetic fields inside the LDCs were characterized using a D^3He exploding pusher proton source for deflectometry measurements at two different energies, 3 MeV and 14.7 MeV [82]. Each target was driven simultaneously by independent 3ω laser beams of 2 kJ energy and 1.5 ns duration focused to $10^{16}\,W/cm^2$. This corresponds to an estimated hot electron temperature of $T_h \sim 16\,$keV [26]. Figure 8 shows a schematic drawing of the configuration of the LDC targets at OMEGA, together with the D^3He capsule as viewed from the proton deflectometry detector.

Figures 9(a) and 9(c) show an example of proton radiography results for 3 MeV and 14.7 MeV, respectively. Accounting for the respective proton energies and the delay between the laser drivers of the LDCs and the pusher, the corresponding probing times are 1.73 ± 0.15 ns and 1.5 ± 0.15 ns, respectively, with respect to the start of the drive beams. The coil plane was imaged into a CR39 detector with a magnification of $M_c = 16$ (the spatial scale given in each image corresponds to the detector plane).

Teardrop-shaped pinch and void structures are visible around the coils, characteristic of multi-kA currents. We measured the currents and charges present in the LDCs by fitting these images to synthetic radiographs obtained with the particle-tracing code PAFIN [79]. An example of these simulations, is shown in Fig. 9(b) for 3 MeV protons, and Fig. 9(d) for 14.7 MeV protons. These radiographs include a current flowing through the targets (6.5 and 8 kA, respectively) and a toroidal static charge distributed around the coils themselves (+4.5 and +8 nC, respectively). The values of both the current and the charge were adjusted iteratively to fit the CR39 data. Note that the features observed in the bottom left corner of the experimental images are not captured by the synthetic radiographs. These features correspond to the plasma between the plates of the LDCs, which is not included in the particle-tracing PAFIN simulations.

While the value of the current has an effect on the size of the inner proton void in the images, this current alone cannot reproduce the outer caustic feature (the halo around the voids), since this is an effect of the electrostatic charge. These two features (void and halo size) can therefore be used to adjust the current and static charge in the targets separately, with an error of $\sim$2 kA, arising mostly from uncertainties in the target geometry. Table I shows the measured currents for both proton energies, compared with the predictions from the described diode model. It can be seen that the model agrees with the measurements (considering the error bars) within 30%.

If the current path was significantly deviated from the wire loop, this would still be apparent from the perpendicular radiographs. Additionally, our targets are designed to minimize the ingress of plasma into the coil region, whether from x-ray photoionization or from the laser focal spot. Moreover, we do not observe extended outer voids or bubbles that could be interpreted as a return current flowing through a surrounding plasma [83].

These results show that currents of order $5-10\,$kA can be driven in mm-sized coils using 3ω light with ns-duration pulses, and give us ground for optimism.

[1] L. Perkins, B. Logan, G. Zimmerman, and C. Werner, Two-dimensional simulations of thermonuclear burn in ignition-scale inertial confinement fusion targets under compressed axial magnetic fields, Phys. Plasmas **20**, 072708 (2013).

[2] D. W. Hill and R. J. Kingham, Enhancement of pressure perturbations in ablation due to kinetic magnetized transport effects under direct-drive inertial confinement fusion relevant conditions, Phys. Rev. E **98**, 021201(R) (2018).

[3] D. Hill, C. Ridgers, R. Kingham, and C. Walsh, Vlasov-Fokker-Planck simulations of pre-magnetized ablating planar targets, Phys. Plasmas **28**, 092708 (2021).

[4] P. Y. Chang, G. Fiksel, M. Hohenberger, J. P. Knauer, R. Betti, F. J. Marshall, D. D. Meyerhofer, F. H. Séguin, and R. D. Petrasso, Fusion Yield Enhancement in Magnetized Laser-Driven Implosions, Phys. Rev. Lett. **107**, 035006 (2011).

[5] R. Jones and W. Mead, The physics of burn in magnetized deuterium-tritium plasmas: Spherical geometry, Nucl. Fusion **26**, 127 (1986).

[6] M. Basko, A. Kemp, and J. Meyer-ter Vehn, Ignition conditions for magnetized target fusion in cylindrical geometry, Nucl. Fusion **40**, 59 (2000).

[7] T. Sano, T. Inoue, and K. Nishihara, Critical Magnetic Field Strength for Suppression of the Richtmyer-Meshkov Instability in Plasmas, Phys. Rev. Lett. **111**, 205001 (2013).

[8] C. Walsh, Magnetized ablative Rayleigh-Taylor instability in three dimensions, Phys. Rev. E **105**, 025206 (2022).

[9] C. Walsh, K. McGlinchey, J. Tong, B. Appelbe, A. Crilly, M. Zhang, and J. Chittenden, Perturbation modifications by pre-magnetisation of inertial confinement fusion implosions, Phys. Plasmas **26**, 022701 (2019).

[10] J. Kline, S. Batha, L. Benedetti, D. Bennett, S. Bhandarkar, L. B. Hopkins, J. Biener, M. Biener, R. Bionta, E. Bond *et al.*, Progress of indirect drive inertial confinement fusion in the United States, Nucl. Fusion **59**, 112018 (2019).

[11] A. Kritcher, C. Young, H. Robey, C. Weber, A. Zylstra, O. Hurricane, D. Callahan, J. Ralph, J. Ross, K. Baker *et al.*, Design of inertial fusion implosions reaching the burning plasma regime, Nat. Phys. **18**, 251 (2022).

[12] A. Zylstra, O. Hurricane, D. Callahan, A. Kritcher, J. Ralph, H. Robey, J. Ross, C. Young, K. Baker, D. Casey *et al.*, Burning plasma achieved in inertial fusion, Nature (London) **601**, 542 (2022).

[13] S. Slutz, M. Herrmann, R. Vesey, A. Sefkow, D. Sinars, D. Rovang, K. Peterson, and M. Cuneo, Pulsed-power-driven cylindrical liner implosions of laser preheated fuel magnetized with an axial field, Phys. Plasmas **17**, 056303 (2010).

[14] M. R. Gomez, S. A. Slutz, A. B. Sefkow, D. B. Sinars, K. D. Hahn, S. B. Hansen, E. C. Harding, P. F. Knapp, P. F. Schmit, C. A. Jennings, T. J. Awe, M. Geissel, D. C. Rovang, G. A. Chandler, G. W. Cooper, M. E. Cuneo, A. J. Harvey-Thompson, M. C. Herrmann, M. H. Hess, O. Johns *et al.*, Experimental Demonstration of Fusion-Relevant Conditions in Magnetized Liner Inertial Fusion, Phys. Rev. Lett. **113**, 155003 (2014).

[15] T. R. Boehly, D. L. Brown, R. S. Craxton, R. L. Keck, J. P. Knauer, J. H. Kelly, T. J. Kessler, S. A. Kumpan, S. J. Loucks, S. A. Letzring, F. J. Marshall, R. L. McCrory, S. F. B. Morse, W. Seka, J. M. Soures, and C. P. Verdon, Initial performance results of the OMEGA laser system, Opt. Commun. **133**, 495 (1997).

[16] J. Davies, D. Barnak, R. Betti, E. Campbell, P.-Y. Chang, A. Sefkow, K. Peterson, D. Sinars, and M. Weis, Laser-driven magnetized liner inertial fusion, Phys. Plasmas **24**, 062701 (2017).

[17] D. Barnak, J. Davies, R. Betti, M. Bonino, E. Campbell, V. Y. Glebov, D. Harding, J. Knauer, S. Regan, A. Sefkow *et al.*, Laser-driven magnetized liner inertial fusion on omega, Phys. Plasmas **24**, 056310 (2017).

[18] E. Hansen, D. Barnak, P.-Y. Chang, R. Betti, E. Campbell, J. Davies, J. Knauer, J. Peebles, S. Regan, and A. Sefkow, Optimization of laser-driven cylindrical implosions on the omega laser, Phys. Plasmas **25**, 122701 (2018).

[19] E. C. Hansen, D. H. Barnak, R. Betti, E. M. Campbell, P.-Y. Chang, J. R. Davies, V. Y. Glebov, J. P. Knauer, J. Peebles, S. P. Regan, and A. B. Sefkow, Measuring implosion velocities in experiments and simulations of laser-driven cylindrical implosions on the OMEGA laser, Plasma Phys. Controlled Fusion **60**, 054014 (2018).

[20] E. Hansen, J. Davies, D. Barnak, R. Betti, E. Campbell, V. Y. Glebov, J. Knauer, L. Leal, J. Peebles, A. Sefkow *et al.*, Neutron yield enhancement and suppression by magnetization in laser-driven cylindrical implosions, Phys. Plasmas **27**, 062703 (2020).

[21] O. Gotchev, J. Knauer, P. Chang, N. Jang, M. Shoup III, D. Meyerhofer, and R. Betti, Seeding magnetic fields for laser-driven flux compression in high-energy-density plasmas, Rev. Sci. Instrum. **80**, 043504 (2009).

[22] C. McGuffey, M. Bailly-Grandvaux, J. Santos, R. Florido, C. Walsh, F. Suzuki-Vidal, F. Beg, A. Calisti, J. Davies, S. Ferri *et al.*, Implementation of laser-driven capacitor coil targets to magnetize an implosion at omega, in *APS Division of Plasma Physics Meeting Abstracts*, Abstract No. NM11.002 (APS, 2020).

[23] M. Bailly-Grandvaux, S. McGuffey, F. Beg, S. Ferri, A. Calisti, J. Davies, R. Florido, M. Gigosos, J. Honrubia, R. Mancini *et al.*, An all-optical platform to characterize strongly magnetized hot dense plasmas at >10 kt, in *APS Division of Plasma Physics Meeting Abstracts*, Abstract No. BO07.005 (APS, 2020).

[24] J. Santos, M. Bailly-Grandvaux, L. Giuffrida, P. Forestier-Colleoni, S. Fujioka, Z. Zhang, P. Korneev, R. Bouillaud, S. Dorard, D. Batani *et al.*, Laser-driven platform for generation and characterization of strong quasi-static magnetic fields, New J. Phys. **17**, 083051 (2015).

[25] K. Law, M. Bailly-Grandvaux, A. Morace, S. Sakata, K. Matsuo, S. Kojima, S. Lee, X. Vaisseau, Y. Arikawa, A. Yogo *et al.*, Direct measurement of kilo-tesla level magnetic field generated with laser-driven capacitor-coil target by proton deflectometry, Appl. Phys. Lett. **108**, 091104 (2016).

[26] V. T. Tikhonchuk, M. Bailly-Grandvaux, J. J. Santos, and A. Poyé, Quasistationary magnetic field generation with a laser-driven capacitor-coil assembly, Phys. Rev. E **96**, 023202 (2017).

[27] J. J. Santos, M. Bailly-Grandvaux, M. Ehret, A. Arefiev, D. Batani, F. Beg, A. Calisti, S. Ferri, R. Florido, P. Forestier-Colleoni *et al.*, Laser-driven strong magnetostatic fields with applications to charged beam transport and magnetized high energy-density physics, Phys. Plasmas **25**, 056705 (2018).

[28] M. Bailly-Grandvaux, J. Santos, C. Bellei, P. Forestier-Colleoni, S. Fujioka, L. Giuffrida, J. Honrubia, D. Batani, R. Bouillaud, M. Chevrot *et al.*, Guiding of relativistic electron beams in dense matter by laser-driven magnetostatic fields, Nat. Commun. **9**, 102 (2018).

[29] C. Walsh, R. Florido, M. Bailly-Grandvaux, F. Suzuki-Vidal, J. P. Chittenden, A. Crilly, M. A. Gigosos, R. Mancini, G. Pérez-Callejo, C. Vlachos *et al.*, Exploring extreme magnetization phenomena in directly driven imploding cylindrical targets, Plasma Phys. Controlled Fusion **64**, 025007 (2022).

[30] A. Casner, T. Caillaud, S. Darbon, A. Duval, I. Thfouin, J. Jadaud, J. LeBreton, C. Reverdin, B. Rosse, R. Rosch *et al.*, LMJ/PETAL laser facility: Overview and opportunities for laboratory astrophysics, High Energy Density Phys. **17**, 2 (2015).

[31] J. Miquel, C. Lion, and P. Vivini, The Laser Mega-Joule: LMJ PETAL status and Program Overview, J. Phys.: Conf. Ser. **688**, 012067 (2016).

[32] J. MacFarlane, VISRAD—A 3-D view factor code and design tool for high-energy density physics experiments, J. Quant. Spectrosc. Radiat. Transfer **81**, 287 (2003).

[33] R. Florido, T. Nagayama, R. Mancini, R. Tommasini, J. Delettrez, S. Regan, V. Smalyuk, R. Rodríguez, and J. Gil, Analysis of time-resolved argon line spectra from omega direct-drive implosions, Rev. Sci. Instrum. **79**, 10E310 (2008).

[34] R. Florido, R. C. Mancini, T. Nagayama, R. Tommasini, J. A. Delettrez, S. P. Regan, and B. Yaakobi, Measurements of core and compressed-shell temperature and density conditions in thick-wall target implosions at the omega laser facility, Phys. Rev. E **83**, 066408 (2011).

[35] R. Florido, R. Mancini, T. Nagayama, R. Tommasini, J. Delettrez, and S. Regan, Time-resolved characterization and energy balance analysis of implosion core in shock-ignition experiments at omega, Phys. Plasmas **21**, 102709 (2014).

[36] H. Chen, T. Ma, R. Nora, M. Barrios, H. Scott, M. Schneider, L. Berzak Hopkins, D. Casey, B. Hammel, L. Jarrott *et al.*, On krypton-doped capsule implosion experiments at the National Ignition Facility, Phys. Plasmas **24**, 072715 (2017).

[37] L. Gao, B. F. Kraus, K. W. Hill, M. B. Schneider, A. Christopherson, B. Bachmann, M. Bitter, P. Efthimion, N. Pablant, R. Betti, C. Thomas, D. Thorn, A. G. MacPhee, S. Khan, R. Kauffman, D. Liedahl, H. Chen, D. Bradley, J. Kilkenny, B. Lahmann, E. Stambulchik *et al.*, Hot Spot Evolution Measured by High-Resolution x-Ray Spectroscopy at the National Ignition Facility, Phys. Rev. Lett. **128**, 185002 (2022).

[38] C. Courtois, C. Robert, D. Bretheau, J. Fariaut, M. Ferri, I. Geoffray, G. Legay, F. Philippe, R. Rosch, G. Soullie, and B. Villette, Supersonic-to-subsonic transition of a radiation wave observed at the LMJ, Phys. Plasmas **28**, 073301 (2021).

[39] B. Zhu, Y. Li, D. Yuan, Y. Li, F. Li, G. Liao, J. Zhao, J. Zhong, F. Xue, S. He *et al.*, Strong magnetic fields generated with a simple open-ended coil irradiated by high power laser pulses, Appl. Phys. Lett. **107**, 261903 (2015).

[40] G. Fiksel, W. Fox, L. Gao, and H. Ji, A simple model for estimating a magnetic field in laser-driven coils, Appl. Phys. Lett. **109**, 134103 (2016).

[41] C. Goyon, B. B. Pollock, D. P. Turnbull, A. Hazi, L. Divol, W. A. Farmer, D. Haberberger, J. Javedani, A. J. Johnson, A. Kemp, M. C. Levy, B. Grant Logan, D. A. Mariscal, O. L. Landen, S. Patankar, J. S. Ross, A. M. Rubenchik, G. F. Swadling, G. J. Williams, S. Fujioka, K. F. F. Law *et al.*, Ultrafast probing of magnetic field growth inside a laser-driven solenoid, Phys. Rev. E **95**, 033208 (2017).

[42] J. Peebles, J. Davies, D. Barnak, T. Cracium, M. Bonino, and R. Betti, Axial proton probing of magnetic and electric fields inside laser-driven coils, Phys. Plasmas **27**, 063109 (2020).

[43] H. Morita, B. B. Pollock, C. S. Goyon, G. J. Williams, K. F. F. Law, S. Fujioka, and J. D. Moody, Dynamics of laser-generated magnetic fields using long laser pulses, Phys. Rev. E **103**, 033201 (2021).

[44] K. Jungwirth, A. Cejnarova, L. Juha, B. Kralikova, J. Krasa, E. Krousky, P. Krupickova, L. Laska, K. Masek, T. Mocek *et al.*, The Prague Asterix Laser system, Phys. Plasmas **8**, 2495 (2001).

[45] J. Zou, C. Blanc, P. Audebert, S. Janicot, A. Sautivet, L. Martin, C. Sauteret, J. Paillard, S. Jacquemot, and F. Amiranoff, Recent progress on LULI high power laser facilities, J. Phys.: Conf. Ser. **112**, 032021 (2008).

[46] M. Hohenberger, W. Theobald, S. Hu, K. Anderson, R. Betti, T. Boehly, A. Casner, D. Fratanduono, M. Lafon, D. Meyerhofer *et al.*, Shock-ignition relevant experiments with planar targets on omega, Phys. Plasmas **21**, 022702 (2014).

[47] O. Renner, M. Šmíd, D. Batani, and L. Antonelli, Suprathermal electron production in laser-irradiated cu targets characterized by combined methods of x-ray imaging and spectroscopy, Plasma Phys. Controlled Fusion **58**, 075007 (2016).

[48] G. Cristoforetti, A. Colaïtis, L. Antonelli, S. Atzeni, F. Baffigi, D. Batani, F. Barbato, G. Boutoux, R. Dudzak, P. Koester *et al.*, Experimental observation of parametric instabilities at laser intensities relevant for shock ignition, Europhys. Lett. **117**, 35001 (2017).

[49] D. Batani, L. Antonelli, F. Barbato, G. Boutoux, A. Colaïtis, J.-L. Feugeas, G. Folpini, D. Mancelli, P. Nicolai, J. Santos *et al.*, Progress in understanding the role of hot electrons for the shock ignition approach to inertial confinement fusion, Nucl. Fusion **59**, 032012 (2018).

[50] S. Zhang, C. Krauland, J. Peebles, J. Li, F. Beg, N. Alexander, W. Theobald, R. Betti, D. Haberberger, E. Campbell *et al.*, Experimental study of hot electron generation in shock ignition relevant high-intensity regime with large scale hot plasmas, Phys. Plasmas **27**, 023111 (2020).

[51] F. Beg, A. Bell, A. Dangor, C. Danson, A. Fews, M. Glinsky, B. Hammel, P. Lee, P. Norreys, and M. Tatarakis, A study of picosecond laser–solid interactions up to 1019 W cm-2, Phys. Plasmas **4**, 447 (1997).

[52] D. F. Price, R. M. More, R. S. Walling, G. Guethlein, R. L. Shepherd, R. E. Stewart, and W. E. White, Absorption of Ultrashort Laser Pulses by Solid Targets Heated Rapidly to Temperatures 1–1000 eV, Phys. Rev. Lett. **75**, 252 (1995).

[53] P. E. O. Chubar and J. Chavanne, A three-dimensional magnetostatics computer code for insertion devices, J. Synchrotron Radiat. **5**, 481(1998).

[54] C. Walsh, J. Chittenden, D. Hill, and C. Ridgers, Extended-magnetohydrodynamics in under-dense plasmas, Phys. Plasmas **27**, 022103 (2020).

[55] J. D. Sadler, C. A. Walsh, and H. Li, Symmetric Set of Transport Coefficients for Collisional Magnetized Plasma, Phys. Rev. Lett. **126**, 075001 (2021).

[56] C. Walsh, J. Sadler, and J. Davies, Updated magnetized transport coefficients: Impact on laser-plasmas with self-generated or applied magnetic fields, Nucl. Fusion **61**, 116025 (2021).

[57] A. Colaïtis, R. K. Follett, J. P. Palastro, I. Igumenschev, and V. Goncharov, Adaptive inverse ray-tracing for accurate and efficient modeling of cross beam energy transfer in hydrodynamics simulations, Phys. Plasmas **26**, 072706 (2019).

[58] J. P. Sauppe, S. Palaniyappan, E. N. Loomis, J. L. Kline, K. A. Flippo, and B. Srinivasan, Using cylindrical implosions to investigate hydrodynamic instabilities in convergent geometry, Matter Radiat. Extremes **4**, 065403 (2019).

[59] S. Palaniyappan, J. Sauppe, B. Tobias, C. Kawaguchi, K. Flippo, A. Zylstra, O. Landen, D. Shvarts, E. Malka, S. Batha *et al.*, Hydro-scaling of direct-drive cylindrical implosions at the omega and the National Ignition Facility, Phys. Plasmas **27**, 042708 (2020).

[60] M. J. Rosenberg, A. A. Solodov, J. F. Myatt, W. Seka, P. Michel, M. Hohenberger, R. W. Short, R. Epstein, S. P. Regan, E. M. Campbell, T. Chapman, C. Goyon, J. E. Ralph, M. A. Barrios, J. D. Moody, and J. W. Bates, Origins and Scaling of Hot-Electron Preheat In Ignition-Scale Direct-Drive Inertial Confinement Fusion Experiments, Phys. Rev. Lett. **120**, 055001 (2018).

[61] S. P. Regan Jr., J. Delettrez, R. Epstein, P. Jaanimagi, B. Yaakobi, V. Smalyuk, F. Marshall, D. Meyerhofer, W. Seka, D. Haynes Jr. *et al.*, Characterization of direct-drive-implosion core conditions on omega with time-resolved ar *K*-shell spectroscopy, Phys. Plasmas **9**, 1357 (2002).

[62] T. Nagayama, R. Mancini, R. Florido, D. Mayes, R. Tommasini, J. Koch, J. Delettrez, S. Regan, and V. Smalyuk, Direct asymmetry measurement of temperature and density spatial distributions in inertial confinement fusion plasmas from pinhole space-resolved spectra, Phys. Plasmas **21**, 050702 (2014).

[63] K. R. Carpenter, R. C. Mancini, E. C. Harding, A. J. Harvey-Thompson, M. Geissel, M. R. Weis, S. B. Hansen, K. Peterson, and G. A. Rochau, Magnetic field impact on the laser heating in MagLIF, Phys. Plasmas **27**, 052704 (2020).

[64] R. Florido, R. Rodríguez, J. M. Gil, J. G. Rubiano, P. Martel, E. Mínguez, and R. C. Mancini, Modeling of population kinetics of plasmas that are not in local thermodynamic equilibrium, using a versatile collisional-radiative model based on analytical rates, Phys. Rev. E **80**, 056402 (2009).

[65] M. E. Sherrill, R. C. Mancini, J. Bailey, A. Filuk, B. Clark, P. Lake, and J. Abdallah, Spectroscopic modeling and characterization of a collisionally confined laser-ablated plasma plume, Phys. Rev. E **76**, 056401 (2007).

[66] M. A. Gigosos, S. Djurović, I. Savić, D. González-Herrero, Z. Mijatović, and R. Kobilarov, Stark broadening of lines from transition between states n = 3 to n = 2 in neutral helium-an experimental and computer-simulation study, Astron. Astrophys. **561**, A135 (2014).

[67] J. Seidel and R. Stamm, Effects of radiator motion on plasma-broadened hydrogen lyman-β, J. Quant. Spectrosc. Radiat. Transfer **27**, 499 (1982).

[68] H. Griem, *Spectral Line Broadening by Plasmas* (Pure and Applied Physics, New York Academic Press, 1974).

[69] M. A. Gigosos, Stark broadening models for plasma diagnostics, J. Phys. D **47**, 343001 (2014).

[70] O. Landoas, V. Yu Glebov, B. Rossé, M. Briat, L. Disdier, T. C. Sangster, T. Duffy, J. G. Marmouget, C. Varignon, X. Ledoux, T. Caillaud, I. Thfoin, and J.-L. Bourgade, Absolute calibration method for laser megajoule neutron yield measurement by activation diagnostics, Rev. Sci. Instrum. **82**, 073501 (2011).

[71] R. Rosch, C. Trosseille, T. Caillaud, V. Allouche, J. L. Bourgade, M. Briat, P. Brunel, M. Burillo, A. Casner, S. Depierreux, D. Gontier, J. P. Jadaud, J. P. Le Breton, P. Llavador, B. Loupias, J. L. Miquel, G. Oudot, S. Perez, J. Raimbourg, A. Rousseau, C. Rousseaux *et al.*, First set of gated x-ray imaging diagnostics for the laser megajoule facility, Rev. Sci. Instrum. **87**, 033706 (2016).

[72] N. Blanchot, G. Béhar, J. Chapuis, C. Chappuis, S. Chardavoine, J. Charrier, H. Coïc, C. Damiens-Dupont, J. Duthu, P. Garcia *et al.*, 1.15 PW–850 J compressed beam demonstration using the PETAL facility, Opt. Express **25**, 16957 (2017).

[73] J. R. Rygg, O. S. Jones, J. E. Field, M. A. Barrios, L. R. Benedetti, G. W. Collins, D. C. Eder, M. J. Edwards, J. L. Kline, J. J. Kroll, O. L. Landen, T. Ma, A. Pak, J. L. Peterson, K. Raman, R. P. J. Town, and D. K. Bradley, 2D X-Ray Radiography of Imploding Capsules at the National Ignition Facility, Phys. Rev. Lett. **112**, 195001 (2014).

[74] E. Dewald, O. Landen, L. Masse, D. Ho, Y. Ping, D. Thorn, N. Izumi, L. Berzak Hopkins, J. Kroll, A. Nikroo *et al.*, X-ray streaked refraction enhanced radiography for inferring inflight density gradients in ICF capsule implosions, Rev. Sci. Instrum. **89**, 10G108 (2018).

[75] D. Raffestin, L. Lecherbourg, I. Lantuéjoul, B. Vauzour, P. Masson-Laborde, X. Davoine, N. Blanchot, J. Dubois, X. Vaisseau, E. d'Humières *et al.*, Enhanced ion acceleration using the high-energy petawatt PETAL laser, Matter Radiat. Extremes **6**, 056901 (2021).

[76] P. Bradford, A. Dearling, M. Ehret, L. Antonelli, N. Booth, D. Carroll, R. Clarke, K. Glize, R. Heathcote, and M. Khan *et al.*, Measuring magnetic fields in laser-driven coils with dual-axis proton deflectometry, Plasma Phys. Controlled Fusion **63**, 084008 (2021).

[77] A. F. A. Bott, L. Chen, G. Boutoux, T. Caillaud, A. Duval, M. Koenig, B. Khiar, I. Lantuéjoul, L. Le-Deroff, B. Reville, R. Rosch, D. Ryu, C. Spindloe, B. Vauzour, B. Villette, A. A. Schekochihin, D. Q. Lamb, P. Tzeferacos, G. Gregori, A. Casner, Inefficient Magnetic-Field Amplification in Supersonic Laser-Plasma Turbulence, Phys. Rev. Lett. **127**, 175002 (2021).

[78] P. Bradford, M. Read, M. Ehret, L. Antonelli, M. Khan, N. Booth, K. Glize, D. Carroll, R. Clarke, R. Heathcote *et al.*, Proton deflectometry of a capacitor coil target along two axes, High Power Laser Sci. Eng. **8**, e11(2020).

[79] M. Ehret, Charged particle beam transport in intense electric and magnetic fields, Master's thesis, Université de Bordeaux and Technische Universitt Darmstadt, 2015, doi: 10.13140/RG.2.1.3820.0806.

[80] D. B. Sinars Jr., M. Sweeney, C. Alexander, D. Ampleford, T. Ao, J. Apruzese, C. Aragon, D. Armstrong, K. Austin, T. Awe *et al.*, Review of pulsed power-driven high energy density physics research on Z at Sandia, Phys. Plasmas **27**, 070501 (2020).

[81] G. Williams, S. Patankar, D. Mariscal, V. Tikhonchuk, J. Bude, C. Carr, C. Goyon, M. Norton, B. Pollock, A. Rubenchik *et al.*, Laser intensity scaling of the magnetic field from a laser-driven coil target, J. Appl. Phys. **127**, 083302 (2020).

[82] C. K. Li, F. H. Séguin, J. R. Rygg, J. A. Frenje, M. Manuel, R. D. Petrasso, R. Betti, J. Delettrez, J. P. Knauer, F. Marshall, D. D. Meyerhofer, D. Shvarts, V. A. Smalyuk, C. Stoeckl, O. L. Landen, R. P. J. Town, C. A. Back, and J. D. Kilkenny, Monoenergetic-Proton-Radiography Measurements of Implosion Dynamics in Direct-Drive Inertial-Confinement Fusion, Phys. Rev. Lett. **100**, 225001 (2008).

[83] A. Chien, L. Gao, S. Zhang, H. Ji, E. Blackman, H. Chen, G. Fiksel, K. Hill, and P. Nilson, Pulse width dependence of magnetic field generation using laser-powered capacitor coils, Phys. Plasmas **28**, 052105 (2021).